Linear Theory Calculations for the Sea Breeze in a Background Wind: The Equatorial Case

TINGTING QIAN, CRAIG C. EPIFANIO, AND FUQING ZHANG

Department of Atmospheric Sciences, Texas A&M University, College Station, Texas

ABSTRACT

The equatorial coastal circulation is modeled in terms of the linear wave response to a diurnally oscillating heat source gradient in a background wind. A diurnal scaling shows that the solution depends on two parameters: a nondimensional coastal width $\mathcal{L}$ and a nondimensional wind speed $\mathcal{U}$. The solutions are interpreted by comparing to the $\mathcal{U} = 0$ theory of Rotunno.

For $\mathcal{U} \neq 0$ the Fourier integral solution consists of three distinct wave branches. Two of these branches correspond to the prior no-wind solution of Rotunno, except with Doppler shifting and associated wave dispersion. The third branch exists only for $\mathcal{U} \neq 0$ and is shown to be broadly similar to flow past a steady heat source or a topographic obstacle. The relative importance of this third branch is determined largely by the parameter combination $\mathcal{U}/\mathcal{L}$. For sufficiently large $\mathcal{U}/\mathcal{L}$ the third branch becomes the dominant part of the solution.

The spatial structures of the three branches are described in terms of group velocity arguments combined with a desingularized quadrature method.

1. Introduction

The sea breeze circulation is an atmospheric response to differential surface heating between the land and the sea. It impacts many atmospheric processes over coastal regions including, but not limited to, the initiation and modulation of thunderstorms, fog, and air pollution. Over the past two centuries since the first known published study on sea breeze by Halley (1686), there have been numerous studies on this subject based on different approaches: observational (Fisher 1960; Davis et al. 1889; Finkele et al. 1995; Miller et al. 2003; Puygrenier et al. 2005), analytical (Jeffreys 1922; Haurwitz 1947; Schmidt 1947; Pierson 1950; Defant 1951; Walsh 1974), numerical (Pearce 1955; Pearce et al. 1956; Estoque 1961; Fisher 1961), and laboratory (Simpson 1997; Cenedese et al. 2000), to name only a few.

Most of the aforementioned studies focus on the local features of the sea breeze and its associated low-level front and density current. However, a few studies have noted that the sea breeze also has a mesoscale gravity wave signature. Sun and Orlanski (1981) were the first to discuss this wave response in terms of a linear sea breeze model with a specified oscillating temperature gradient. The idea was later explored in greater detail by Rotunno (1983, hereafter R83), who considered the linear theory for the problem of an oscillating heat source in a resting background state. R83 showed that the solution is a propagating wave response whenever the Coriolis parameter is smaller than the diurnal frequency (i.e., equatorward of 30° latitude). Yan and Anthes (1987) extended many of these ideas to a nonlinear context using numerical simulations. Dalu and Pielke (1989) extended the linear theory of R83 to include aperiodic heat forcing. More recently, observational studies such as Yang and Slingo (2001) and Mapes et al. (2003a,b) have suggested that such diurnal coastal gravity waves may play a role in initiating convection far offshore. Wave disturbances forced by diurnal heating were also proposed as a mechanism for convective initiation over the continental United States in summer (e.g., Zhang and Koch 2000; Koch et al. 2001; Carbone et al. 2002).

The current study seeks to extend the linear theory of R83 by including the effect of background wind on

Corresponding author address: Craig C. Epifanio, Department of Atmospheric Sciences, Texas A&M University, Box 3150, College Station, TX 77843.
E-mail: cepi@tamu.edu

the sea breeze wave response, which, to the best of our knowledge, has never been explored analytically. Section 2 gives the basic equations and the associated Fourier transform solution. Section 3 revisits the no-wind linear theory of R83. The solution with the effect of the background wind added is provided in section 4. The spatial structure of the sea breeze wave response is discussed in terms of group propagation in section 5. A summary is presented in section 6.

2. Basic methods

a. Basic equations and scaling parameters

We consider a 2D Boussinesq and hydrostatic flow as linearized about a uniform background state with background wind speed U. Attention is limited to the equatorial case so that the Coriolis parameter is taken to be zero. The primitive equations in dimensional form (as indicated by asterisks) are then given by

$$\frac{\partial u^*}{\partial t^*} + U\frac{\partial u^*}{\partial x^*} = -\frac{\partial P^*}{\partial x^*}, \tag{1}$$

$$\frac{\partial P^*}{\partial z^*} = b^*, \tag{2}$$

$$\frac{\partial b^*}{\partial t^*} + U\frac{\partial b^*}{\partial x^*} + N^2 w^* = Q^*, \quad \text{and} \tag{3}$$

$$\frac{\partial u^*}{\partial x^*} + \frac{\partial w^*}{\partial z^*} = 0, \tag{4}$$

where u^* and w^* are the disturbance velocities in the x^* and z^* directions, P^* is the Boussinesq disturbance pressure, b^* is the buoyancy, and N is the background state static stability. Here, Q^* is the diabatic heating profile, which in principle includes both the turbulent transfer of heat by boundary layer eddies and the effects of radiation. Following R83, we simplify the problem as much as possible by letting Q^* be strictly periodic in time. Specifically,

$$Q^* = \frac{Q_0}{\pi}\left(\frac{\pi}{2} + \tan^{-1}\frac{x^*}{L}\right)\exp\left(-\frac{z^*}{H}\right)\cos(\omega t^*), \tag{5}$$

where Q_0, L, H, and ω are the constant heating amplitude, half-width of the coastal zone, heating depth, and diurnal frequency, respectively. Here the coastline is at $x^* = 0$ with land to the right ($x^* > 0$) and sea to the left.

The lower boundary is assumed flat so that $w^* = 0$ at $z^* = 0$. Apart from the diurnal oscillations in b^* and P^* over land, the disturbance is assumed to vanish as

$|x^*| \to \infty$.[1] The domain is unbounded aloft with a radiation condition applied as $z^* \to \infty$.

The system is nondimensionalized using scaling factors derived from the $U = 0$ solution of R83. Specifically, R83 showed that for a resting background state, the depth scale of the disturbance is set externally by the vertical scale of heating (i.e., by H). The horizontal scale is then given by $H/\delta = NH/\omega$, where $\delta = \omega/N$ is the geometric aspect ratio (depth/length) set by the associated gravity wave dispersion relation (see R83). The time scale is determined by the period of the heating forcing. The rest of the scales then follow from the dominant balances in (1)–(4). The scaling factors are

$$x^* = \frac{NH}{\omega}x, \quad z^* = Hz, \quad t^* = \frac{t}{\omega},$$

$$Q^* = Q_0 Q, \quad u^* = \frac{Q_0}{N\omega}u, \quad w^* = \frac{Q_0}{N^2}w,$$

$$b^* = \frac{Q_0}{\omega}b, \quad \text{and} \quad P^* = \frac{Q_0 H}{\omega}P,$$

where again the asterisks indicate dimensional quantities. Substituting the scaling factors into (1)–(5), we have a set of nondimensional equations:

$$\frac{\partial u}{\partial t} + \mathcal{U}\frac{\partial u}{\partial x} = -\frac{\partial P}{\partial x}, \tag{6}$$

$$\frac{\partial P}{\partial z} = b, \tag{7}$$

$$\frac{\partial b}{\partial t} + \mathcal{U}\frac{\partial b}{\partial x} + w = Q, \quad \text{and} \tag{8}$$

$$\frac{\partial u}{\partial x} + \frac{\partial w}{\partial z} = 0, \quad \text{with} \tag{9}$$

$$Q = \frac{1}{\pi}\left(\frac{\pi}{2} + \tan^{-1}\frac{x}{\mathcal{L}}\right)\exp(-z)\cos(t), \tag{10}$$

where $\mathcal{U} = U/NH$ is the nondimensional background wind speed[2] and $\mathcal{L} = \omega L/NH$ is the nondimensional

---

[1] The basis for this assumption is that the velocity field responds only to gradients in the heating rather than the heating itself. To see this, consider a problem in which the heat source extends uniformly to infinity in both directions in x. The pressure and buoyancy in this problem both oscillate, but no horizontal gradients are formed and no motion occurs [cf. (1) and (4), or equivalently (12)]. The same holds for our problem as $x \to \infty$.

[2] Physically, the parameter $\mathcal{U}$ measures the size of the background wind speed relative to the characteristic phase speeds present in the $U = 0$ case. Because the depth scale for the R83 solution is H, the relevant phase speed is then NH. The combination U/NH is also sometimes referred to as the *thermal Froude number* (e.g., Lin 2007, chapter 6).

half-width of the coastal zone. It is obvious that the only two control parameters for the nondimensional problem are then $\mathcal{U}$ and $\mathcal{L}$.

Solutions are sought in terms of a streamfunction ψ, defined by

$$u = \frac{\partial \psi}{\partial z} \quad \text{and} \quad w = -\frac{\partial \psi}{\partial x}. \qquad (11)$$

Reducing (6)–(9) to a single equation in ψ then gives

$$\left(\frac{\partial}{\partial t} + \mathcal{U}\frac{\partial}{\partial x}\right)^2 \frac{\partial^2 \psi}{\partial z^2} + \frac{\partial^2 \psi}{\partial x^2} = -\frac{\partial Q}{\partial x}. \qquad (12)$$

b. Fourier transform solution

The Fourier transform of (12) gives

$$\left(\frac{\partial}{\partial t} + i\mathcal{U}\kappa\right)^2 \frac{\partial^2 \tilde{\psi}}{\partial z^2} - \kappa^2 \tilde{\psi} = -e^{-\kappa\mathcal{L}}e^{-z}\frac{e^{it} + e^{-it}}{2}, \qquad (13)$$

where κ is the nondimensional horizontal wavenumber and $\tilde{\psi}$ is the Fourier transform of ψ defined by

$$\tilde{\psi}(\kappa, z, t) = \int_{-\infty}^{\infty} \psi(x, z, t)e^{-i\kappa x}dx.$$

Solutions are obtained by first decomposing the forcing into the e^{it} and e^{-it} modes and then solving for each mode independently. Writing the solution for a given mode in the form

$$\tilde{\psi}(\kappa, z, t) = \hat{\psi}(\kappa, z)e^{\pm it} \qquad (14)$$

and substituting into (13) then gives

$$\hat{\omega}^2 \frac{d^2\hat{\psi}}{dz^2} + \kappa^2 \hat{\psi} = \frac{1}{2}e^{-\kappa\mathcal{L}}e^{-z}, \qquad (15)$$

where $\hat{\omega} = \pm 1 + \mathcal{U}\kappa$ is the dimensionless intrinsic frequency, with the $\pm$ matching that given in (14).

Because ψ is real, we can specify κ so as to always be positive. The e^{it} and e^{-it} modes then correspond to leftward- and rightward-propagating waves relative to the ground, respectively. The phase speed of the waves is given by $c_x = \mp 1/\kappa$, showing that longer waves propagate faster than shorter waves.

For concreteness we restrict attention to the case $\mathcal{U} \geq 0$. (The $\mathcal{U} < 0$ case is simply the reflection about the $x = 0$ axis.) In the flow-relative (or intrinsic) frame, the specified heat source is then seen as propagating to the left at speed $\mathcal{U}$, which causes the Fourier modes to be Doppler shifted. For leftward-moving (or e^{it}) modes, the intrinsic propagation is faster than the ground-relative value, implying that $\hat{\omega}$ for these modes is greater than the di-

urnal frequency (i.e., $\hat{\omega} > 1$). For rightward-moving (or e^{-it}) modes with phase speeds greater than $\mathcal{U}$ (i.e., long waves with $1/\kappa > \mathcal{U}$), the intrinsic propagation is slower than the ground-relative value so that the intrinsic frequency satisfies $-1 < \hat{\omega} < 0$. Rightward-moving waves with phase speeds less than $\mathcal{U}$ (i.e., short waves with $1/\kappa < \mathcal{U}$) are seen as leftward moving in the intrinsic frame and thus have $\hat{\omega} > 0$.

The solutions to (15) are obtained in terms of Green's functions in the vertical with a radiation condition applied aloft, resulting in

$$\hat{\psi}(\kappa, z) = \begin{cases} -e^{-\kappa\mathcal{L}}(e^{imz} - e^{-z})/(2\hat{\omega}^2 + 2\kappa^2), & \hat{\omega} > 0, \\ -e^{-\kappa\mathcal{L}}(e^{-imz} - e^{-z})/(2\hat{\omega}^2 + 2\kappa^2), & \hat{\omega} < 0, \end{cases} \qquad (16)$$

where $m = \kappa/|\hat{\omega}|$ is the nondimensional vertical wavenumber (defined to always be positive). Note that the selection of the vertical mode is determined by the intrinsic phase propagation rather than the phase propagation relative to the ground. Leftward-propagating modes in the intrinsic frame ($\hat{\omega} > 0$) all have negative phase tilts (i.e., e^{imz} modes) whereas rightward-propagating modes in the intrinsic frame ($\hat{\omega} < 0$) all have positive phase tilts (e^{-imz} modes). The solution for a given mode then follows from (14), with the full solution to (13) being the superposition of the e^{it} and e^{-it} cases.

According to (11), the Fourier transform for w is given by $\tilde{w} = -i\kappa\tilde{\psi}$, whereas the solution for $\tilde{u}$ follows from the appropriate z derivatives of (16).

3. Review: The no-wind case

The solution for $\mathcal{U} = 0$ has been described in some detail by R83. Here the basic properties of this solution are reviewed in preparation for the $\mathcal{U} \neq 0$ case described in section 4.

a. Computation

Setting $\mathcal{U} = 0$ in (12) leads to the Fourier solution

$$\psi = I_1 + I_2, \quad \text{where}$$

$$I_1 = -\frac{1}{2\pi}\int_0^\infty \frac{e^{-\kappa\mathcal{L}}}{\kappa^2 + 1}(e^{imz} - e^{-z})e^{i(\kappa x + t)}d\kappa \quad \text{and} \qquad (17)$$

$$I_2 = -\frac{1}{2\pi}\int_0^\infty \frac{e^{-\kappa\mathcal{L}}}{\kappa^2 + 1}(e^{-imz} - e^{-z})e^{i(\kappa x - t)}d\kappa \qquad (18)$$

consist of the leftward- and rightward-propagating modes, respectively. It should be understood that only the real parts in (17) and (18) are physically meaningful. As in section 2, the vertical wavenumber m is defined so that

$m = \kappa$. Solutions for u and w follow from the derivatives of (17) and (18), as described in section 2.

Inspection of the integrals shows that the integrands in (17) and (18) are well behaved everywhere along the real κ axis. Numerical computation of the integrals is thus straightforward and follows methods outlined for the I_1 case in the appendix.

b. Basic morphology

With $\mathcal{U} = 0$ the only nondimensional control parameter for the flow is the coastal width $\mathcal{L}$, with the figures in R83 being for $\mathcal{L} = 0.2$. An analogous calculation for $\mathcal{L} = 0.1$ is shown in Fig. 1. The solution is localized along two parallel wave beams with centers at $z = x$ and $z = -x$. As shown by R83, the slopes of these wave beams correspond to energy propagation for diurnal gravity modes. In the present case the energy propagates away from the heat source gradient near $x = 0$.

With $\mathcal{L} = 0.1$, the vertical scale of the wave beams is set by the heating depth, while the dominant horizontal scale is obtained through the aspect ratio δ (as in section 2). These length and depth scales form the basis of our scaling, so that in nondimensional terms both the width and depth of the wave beams are roughly one. The phase lines of the modes propagate downward as time evolves (as seen in Figs. 1a,c or 1b,d). Surprisingly, the cross-coastline winds are nearly π out of phase with the heating. Broadly speaking, this π phase lag results from the $\pi/2$ lag between the heat source and the temperature (and hence pressure) gradient, as well as from the $\pi/2$ lag between the pressure gradient and the wind. A detailed explanation can be found in R83.

Finally, Figs. 1e,f exhibit the decomposition of the horizontal velocity u into leftward- and rightward-propagating modes. As expected, the branch at $x > 0$ consists of rightward-propagating modes, whereas the branch at $x < 0$ consists of leftward-propagating modes.

c. $\mathcal{L}$ dependence

For reference, suppose we pick characteristic dimensional values of $N = 0.01 \text{ s}^{-1}$, $\omega = 2\pi \text{ day}^{-1}$, $H = 800 \text{ m}$, and $L = 10 \text{ km}$. Combining these then gives a characteristic nondimensional coastal width of $\mathcal{L} \sim 0.1$, as considered above. But in reality, $\mathcal{L}$ might be larger or smaller than this value, depending on the values of N, H, and L in a given case.

The sensitivity of the $\mathcal{U} = 0$ solution to changes in $\mathcal{L}$ is illustrated by Figs. 1c and 2. As expected, for small $\mathcal{L}$ (Figs. 2a and 1c) the depth scale is set by the heating depth whereas the length scale follows from the dynamical aspect ratio. The result is that the dominant

horizontal and vertical scales are both roughly independent of $\mathcal{L}$ for small $\mathcal{L}$, with the dominant wavenumber given by $m = \kappa \simeq 1$. However, according to (17) and (18) the power at this dominant wavenumber varies roughly as $e^{-\mathcal{L}}$, so that as $\mathcal{L}$ increases the amplitude of the solution becomes smaller (cf. Figs. 1c and 2a). As $\mathcal{L}$ is made still larger (as shown in Fig. 2b with $\mathcal{L} = 0.5$ and Fig. 2c with $\mathcal{L} = 1$), the scales start to change so that the horizontal scale is set by $\mathcal{L}$ while the vertical scale follows from the aspect ratio, and the amplitude continues to decrease.

4. Adding the background wind

The character of sea breeze in a background wind is examined in this section. As will be seen, the Doppler shifting of the modes can lead to significant differences from the $\mathcal{U} = 0$ solution.

a. Computation

With $\mathcal{U} \neq 0$ in (16), the Fourier integral solution becomes

$$\psi = I_1 + I_2 + I_3,$$

where the three different branches are defined by the following:

Left-moving waves with $\hat{\omega} = 1 + \mathcal{U}\kappa > 0$; that is,

$$I_1 = -\frac{1}{2\pi} \int_0^\infty \frac{e^{-\kappa\mathcal{L}}}{\kappa^2 + (1 + \mathcal{U}\kappa)^2}(e^{imz} - e^{-z})e^{i(\kappa x + t)}d\kappa; \tag{19}$$

Right-moving waves with $\hat{\omega} = -1 + \mathcal{U}\kappa < 0$; that is,

$$I_2 = -\frac{1}{2\pi} \int_0^{\kappa_\mathcal{U}} \frac{e^{-\kappa\mathcal{L}}}{\kappa^2 + (\mathcal{U}\kappa - 1)^2}(e^{-imz} - e^{-z})e^{i(\kappa x - t)}d\kappa; \text{ and} \tag{20}$$

Right-moving waves with $\hat{\omega} = -1 + \mathcal{U}\kappa > 0$; that is,

$$I_3 = -\frac{1}{2\pi} \int_{\kappa_\mathcal{U}}^\infty \frac{e^{-\kappa\mathcal{L}}}{\kappa^2 + (\mathcal{U}\kappa - 1)^2}(e^{imz} - e^{-z})e^{i(\kappa x - t)}d\kappa. \tag{21}$$

The cutoff wavenumber $\kappa_\mathcal{U} = 1/\mathcal{U}$ in (20) and (21) is the critical wavenumber at which the rightward-propagating phase speed matches the background wind speed. The vertical wavenumber is $m = \kappa/|\hat{\omega}|$ for all three branches.
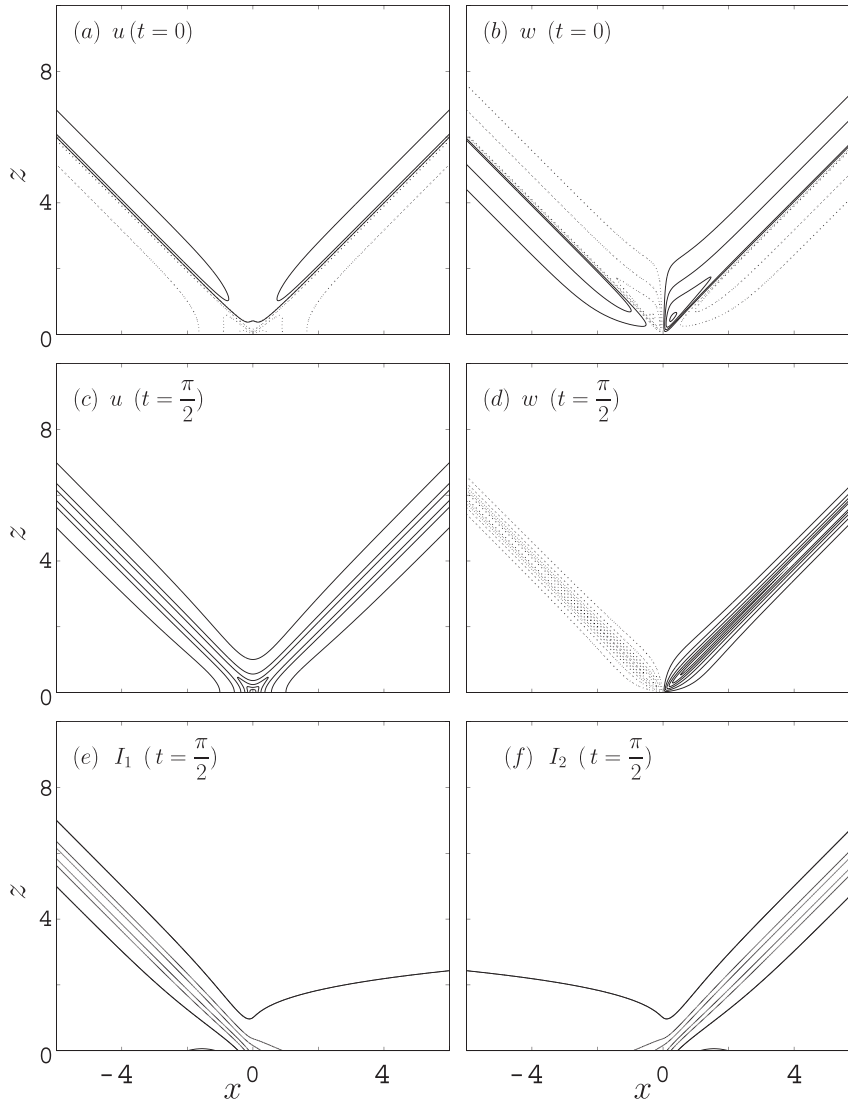
FIG. 1. (a),(c) Horizontal and (b),(d) vertical velocity components for $\mathcal{U} = 0$ and $\mathcal{L} = 0.1$, with horizontal velocity u at times $t =$ (a) 0 and (c) $\pi/2$ [contour interval (c.i.) = 0.1; solid contours, positive; dotted contours, negative] and vertical velocity w at times $t =$ (b) 0 and (d) $\pi/2$ (c.i. = 0.05 with zero contour straddled). (e) Leftward-moving (or I_1) and (f) rightward-moving (or I_2) parts of u at $t = \pi/2$. Solutions for $t = \pi$ and $3\pi/2$ are simply the negatives of the solutions at $t = 0$ and $\pi/2$, respectively.

It is worth noting that the integrands in both (20) and (21) become singular in the limit $\kappa \to \kappa_{\mathcal{U}}$ because $\hat{\omega} = -1 + \mathcal{U}\kappa \to 0$ in this limit, so that $m \to \infty$. The result is that the $e^{\pm imz}$ terms oscillate infinitely fast with κ in this limit, which in turn complicates the numerical computation of the Fourier integrals. This is especially true for the horizontal velocity $u = \partial\psi/\partial z$ because the vertical derivative produces an amplitude singularity as well as a singular oscillation. Our approach to overcoming these problems is based on a method first proposed by Muraki (2000) in the context of flow past to-

pography. Broadly speaking, the basis of the method is to first remove the singular oscillation with an analytically integrable function and to then apply the numerical quadrature only to the difference integral. Details of the method can be found in the appendix.

b. Basic inferences

To simplify terminology, we refer to the flow pattern illustrated by Fig. 1 as the R83 pattern and to the wavenumbers near $m \sim 1$ (which dominate the $\mathcal{U} = 0$
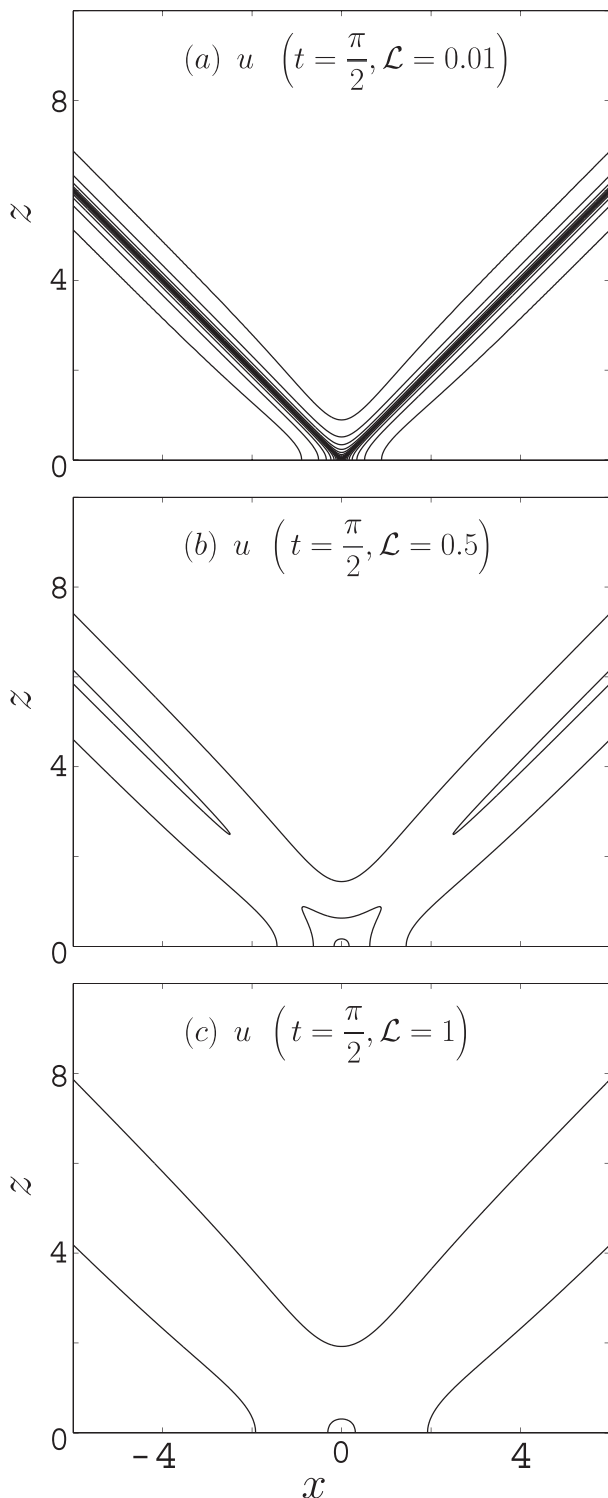
FIG. 2. Horizontal velocity u at time $t = \pi/2$ with $\mathcal{U} = 0$ and coastal width $\mathcal{L}$ = (a) 0.01, (b) 0.5, and (c) 1 (contours as in Fig. 1).

solution) as the R83 modes. Inspection of (19)–(21) then suggests two main impacts of the background wind: (i) the R83 modes in I_1 and I_2 will become Doppler shifted and dispersive and (ii) the contribution from I_3 will become stronger as $\mathcal{U}$ increases. Here we briefly consider the $\mathcal{U}$ and $\mathcal{L}$ dependence of these effects.

For sufficiently small $\mathcal{U}$, the cutoff wavenumber $\kappa_{\mathcal{U}}$ in (21) is relatively large and the contribution from I_3 is therefore negligible. The two branches I_1 and I_2 in this limit are then analogous to the $\mathcal{U} = 0$ cases in (17) and (18), except that the R83 modes in the branches will be Doppler shifted to higher and lower intrinsic frequencies. Because the scale of the R83 modes is roughly $\kappa \approx m \sim 1$, the extent of this frequency shifting will be determined primarily by $\mathcal{U}$ (and not by $\mathcal{L}$).

As $\mathcal{U}$ increases, $\kappa_{\mathcal{U}}$ becomes smaller and the I_3 modes will gradually become more important. Because $\hat{\omega}$ for these modes is dominated by $\mathcal{U}\kappa$ (instead of by the diurnal frequency), the general behavior of these I_3 modes is expected to be broadly similar to flow past a stationary heat source (or equivalently to flow past topography). As in the stationary heating or topography problems, we expect that the dominant w forcing for these modes will be near $\kappa \sim 1/\mathcal{L}$. A reasonable expectation then is that the I_3 modes will become important only once $\kappa_{\mathcal{U}} < 1/\mathcal{L}$, or equivalently $\mathcal{U}/\mathcal{L} > 1$.

c. $\mathcal{U}$ dependence

The $\mathcal{U}$ dependence of the solution for the case $\mathcal{L} = 0.1$ is illustrated in Figs. 3 and 4 . Figure 3 shows the vertical velocity for increasing values of $\mathcal{U}$; Fig. 4 shows the decomposition into I_1, I_2, and I_3 modes. For reference, thick solid lines in Fig. 4 show the raypaths for the $\mathcal{U} = 0$ solution, while the thick dashed lines show the raypaths for the R83 modes (i.e., modes with $m \sim 1$) as Doppler shifted for $\mathcal{U} \neq 0$. Details of the raypath calculations can be found in section 5.

As expected, for $\mathcal{U} = 0.075$ the solution in Fig. 3a is composed primarily of the I_1 and I_2 branches (see Figs. 4a–c). For I_1, the Doppler shifting of the modes leads to higher intrinsic frequencies, and the phase lines and raypaths for this branch are thus more steeply inclined to the vertical than for $\mathcal{U} = 0$. The energy of the branch is also more widely dispersed, with shorter wavelengths having steeper energy propagation (see discussion in section 5). By contrast, the I_2 modes are shifted to lower $|\hat{\omega}|$ and the phase lines and raypaths are therefore less steeply inclined (Fig. 4b).

With increasing $\mathcal{U}$ the raypaths for the I_1 and I_2 R83 modes become further rotated from the $\mathcal{U} = 0$ case (see the second through fourth rows in Fig. 4). However, a more significant change is the gradual appearance of the
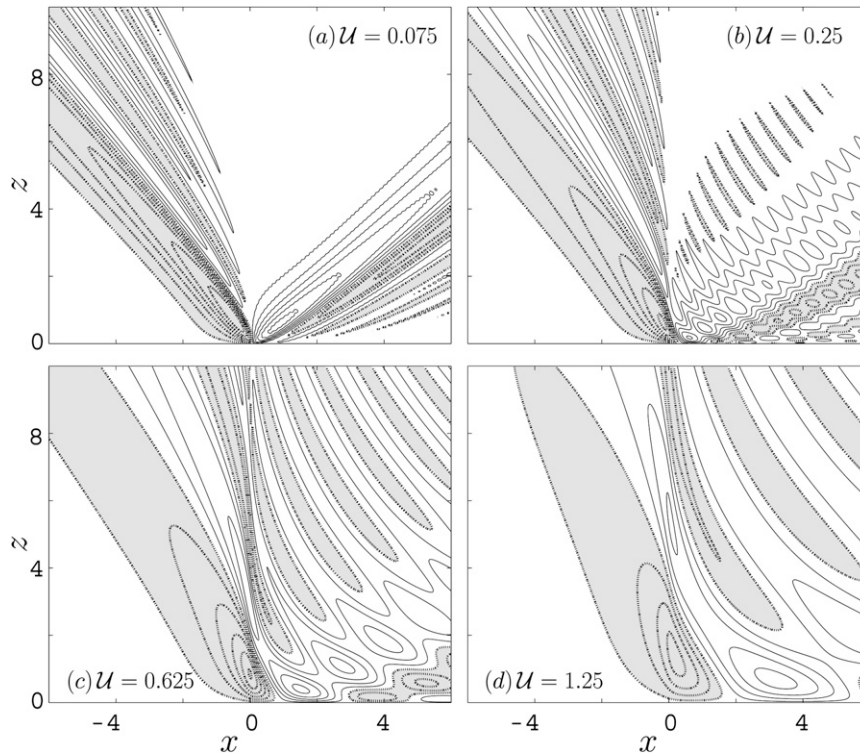
FIG. 3. Vertical velocity w at $t = \pi/2$ with $\mathcal{L} = 0.1$ and $\mathcal{U} = $ (a) 0.075, (b) 0.25, (c) 0.625, and (d)
1.25 (c.i. = 0.04; solid lines, positive; dotted lines and shaded, negative).

I_3 branch. The I_3 branch is composed of rightward-propagating waves (relative to the ground) with negative phase tilts, and the character of this branch is thus fundamentally different from I_1 and I_2. Qualitatively, the wave pattern for I_3 more closely resembles flow past a steady heat source or a topographic obstacle (see, e.g., Lin 2007, chapters 5 and 6) than it does a stationary diurnal oscillation as in Fig. 1.

As suggested in section 4b, the I_3 modes in Fig. 4 only become significant once $\mathcal{U}/\mathcal{L}$ is sufficiently large (roughly $\mathcal{U}/\mathcal{L} \approx 2$ in present case). For $\mathcal{U} = 0.25$ and $\mathcal{U} = 0.625$ the flow consists of relatively high-wavenumber (because $\kappa_\mathcal{U}$ is still relatively large) I_3 modes superimposed on a Doppler-tilted R83 pattern (see Figs. 3b,c and the second and third rows of Fig. 4). However, by $\mathcal{U} = 1.25$ (or $\mathcal{U}/\mathcal{L} = 12.5$) the I_3 branch is the dominant part of the solution.

Figure 5 shows the horizontal velocity u corresponding to the vertical velocity shown in Fig. 3. The general trend in the solution with increasing $\mathcal{U}$—Doppler tilting of the R83 modes and the gradual increase in I_3—is the same as for vertical velocity. The main difference is that for large $\mathcal{U}$, the I_3 part of the u disturbance is localized downstream and closer to the ground (cf. Figs. 3d and 5d). Further discussion of this point is given in section 5c. Note that the $\mathcal{U}$ dependence in Figs. 3 and 5 explains

some of the asymmetric features observed in previous analytical and modeling studies, such as that of Walsh (1974).

d. Time evolution

Figure 6 displays the time evolution for both the decomposition and total vertical velocity fields with $\mathcal{U} = 0.875$ and $\mathcal{L} = 0.1$. As in the $\mathcal{U} = 0$ case (cf. Fig. 1), the phase lines in the I_1 and I_2 branches (Figs. 6a,d,g) propagate downward through the respective wave envelopes with time. However, in the ground-relative frame the I_3 modes are rightward propagating, and the phase lines for the I_3 branch (Figs. 6b,e,h) thus propagate upward and downstream. The phase evolution for the total fields thus has elements of both these behaviors.

e. $\mathcal{L}$ dependence

The $\mathcal{L}$ dependence of the I_1, I_2, and I_3 modes at fixed $\mathcal{U} = 0.5$ is illustrated by Fig. 7. As expected, for the I_1 and I_2 branches the Doppler tilting and general wave patterns are essentially independent of $\mathcal{L}$ (for sufficiently small $\mathcal{L}$). However, the amplitudes of the two branches increase as $\mathcal{L}$ decreases, much as in the $\mathcal{U} = 0$ case of section 3c. For the I_3 branch the disturbance
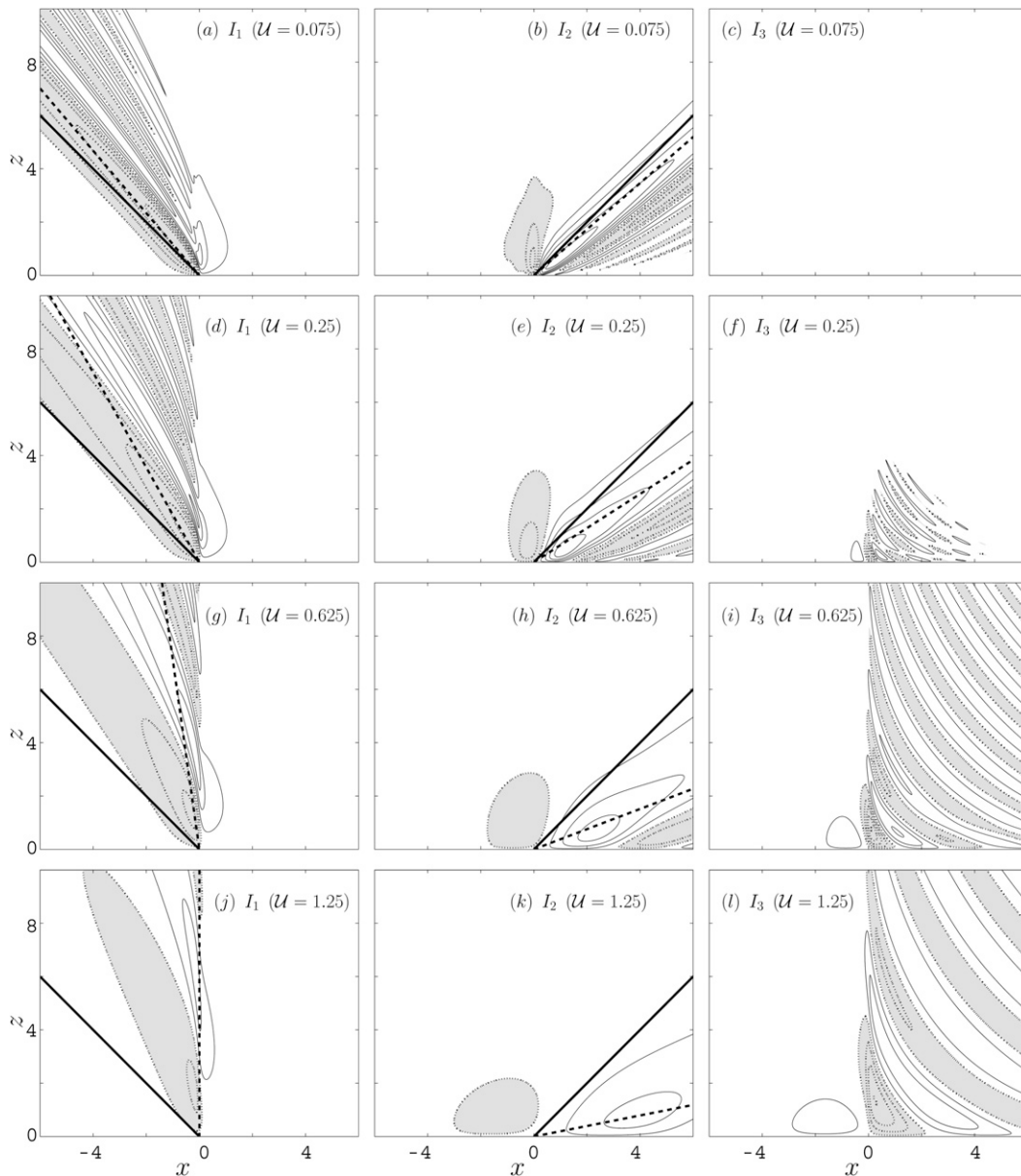
FIG. 4. I_1, I_2, and I_3 branches of vertical velocity w (c.i. = 0.04) at $t = \pi/2$ with $\mathcal{L} = 0.1$ and different background wind $\mathcal{U}$. (a) I_1, (b) I_2 and (c) I_3 with $\mathcal{U} = 0.075$. (d)–(l) As in (a)–(c), but with (d)–(f) $\mathcal{U} = 0.25$, (g)–(i) $\mathcal{U} = 0.625$, and (j)–(l) $\mathcal{U} = 1.25$. Thick solid lines for I_1 and I_2 show the raypaths for the $\mathcal{U} = 0$ solution of R83. Thick dashed lines show raypaths for the Doppler-shifted R83 modes.

becomes relatively more important (compared to I_1 and I_2) as $\mathcal{L}$ decreases so that $\mathcal{U}/\mathcal{L}$ increases.[3] As in Fig. 4, the noticeable onset of the I_3 branch occurs roughly near $\mathcal{U}/\mathcal{L} \approx 2$.

Taken together, the results shown in Figs. 3–7 generally reinforce the basic inferences made in section 4b—specifically, that the I_1 and I_2 branches are determined largely by $\mathcal{U}$ whereas the importance of the I_3 branch (relative to I_1 and I_2) depends primarily on $\mathcal{U}/\mathcal{L}$. Various different values of $\mathcal{U}$ and $\mathcal{L}$ can thus lead to various combinations of these two effects (as seen by comparing Figs. 4 and 7). In the following section we consider the overall spatial structures of these three branches in greater detail.

---

[3] To see this, consider the changes in amplitudes for the three branches as $\mathcal{L}$ decreases. Between $\mathcal{L} = 0.2$ and $\mathcal{L} = 0.04$ in Fig. 7, the amplitudes of the I_1 and I_2 branches increase by 50%, whereas the increase in the I_3 amplitude is nearly a factor of 3.
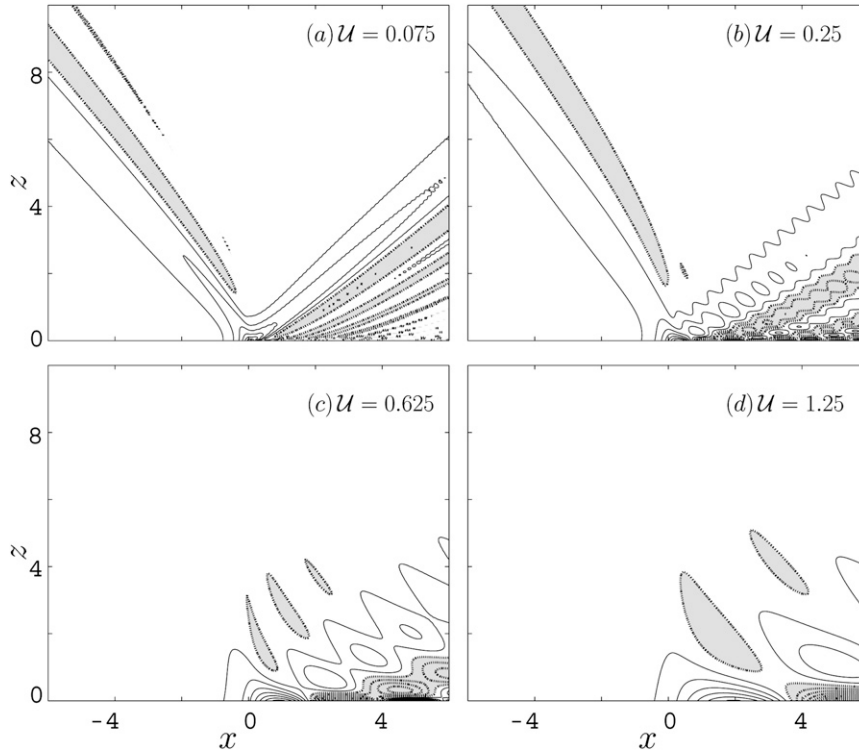
FIG. 5. Horizontal velocity u at $t = \pi/2$ with $\mathcal{L} = 0.1$ and $\mathcal{U} =$ (a) 0.075, (b) 0.25, (c) 0.625, and (d)
1.25 (c.i. = 0.1; solid lines, positive; dotted lines and shaded, negative).

5. Group propagation and wave scales

The present section explores the structure and spatial scales of the three branches in terms of group propagation arguments.

Generally, the solution (19)–(21) consists of Fourier wave modes of the form of $\exp(i\kappa x + i\lambda z + i\sigma t)$, where in the present case $\lambda = \pm m$, $\sigma = \pm 1$, and κ is positive. The dispersion relation for these Fourier modes can be described uniformly by

$$\sigma + \mathcal{U}\kappa = \frac{\kappa}{\lambda}, \qquad (22)$$

where the sign of λ accounts for the direction of intrinsic phase propagation. The corresponding group propagation is given by

$$c_{gx} = -\frac{\partial \sigma}{\partial \kappa} = -\frac{1}{\lambda} + \mathcal{U} \quad \text{and} \quad c_{gz} = -\frac{\partial \sigma}{\partial \lambda} = \frac{\kappa}{\lambda^2},$$

which implies raypaths of slope

$$\tan \theta = \frac{c_{gz}}{c_{gx}} = \frac{\kappa}{-\lambda + \mathcal{U}\lambda^2}, \qquad (23)$$

where θ is the angle between the raypath and the positive x axis. Note that for given $\mathcal{U}$ the raypath for fixed κ and λ is a straight line (i.e., θ is fixed).

Because σ is known, (22) and (23) can be combined to give the angle of the raypath in terms of either κ or λ independently. The result is

$$\tan \theta = -\frac{(\sigma + \mathcal{U}\kappa)^2}{\sigma} \quad \text{or} \quad \tan \theta = -\frac{\sigma}{(1 - \mathcal{U}\lambda)^2}. \quad (24)$$

a. I_1 modes

For the I_1 branch we have $\sigma = 1$ and $\lambda = m > 0$. Solving (24) for the horizontal and the vertical wavenumbers then gives

$$\kappa = (\sqrt{-\tan \theta} - 1)/\mathcal{U} \quad \text{and} \quad m = (1 - \sqrt{-1/\tan \theta})/\mathcal{U}, \qquad (25)$$

where θ must satisfy $\pi/2 < \theta < 3\pi/4$ to give both positive κ and m. Inspection of (25) shows that both κ and m are zero at $\theta = 3\pi/4$ and increase as θ decreases toward the vertical. Shorter horizontal waves thus have more steeply inclined raypaths and smaller vertical wavelengths (cf. Fig. 4). The largest vertical wavenumber of $m = 1/\mathcal{U}$ occurs at $\theta = \pi/2$.

As described in section 4, for small and moderate values of $\mathcal{U}$ we expect I_1 to be dominated by modes with $m \sim 1$ (i.e., the R83 modes). The raypath for these R83
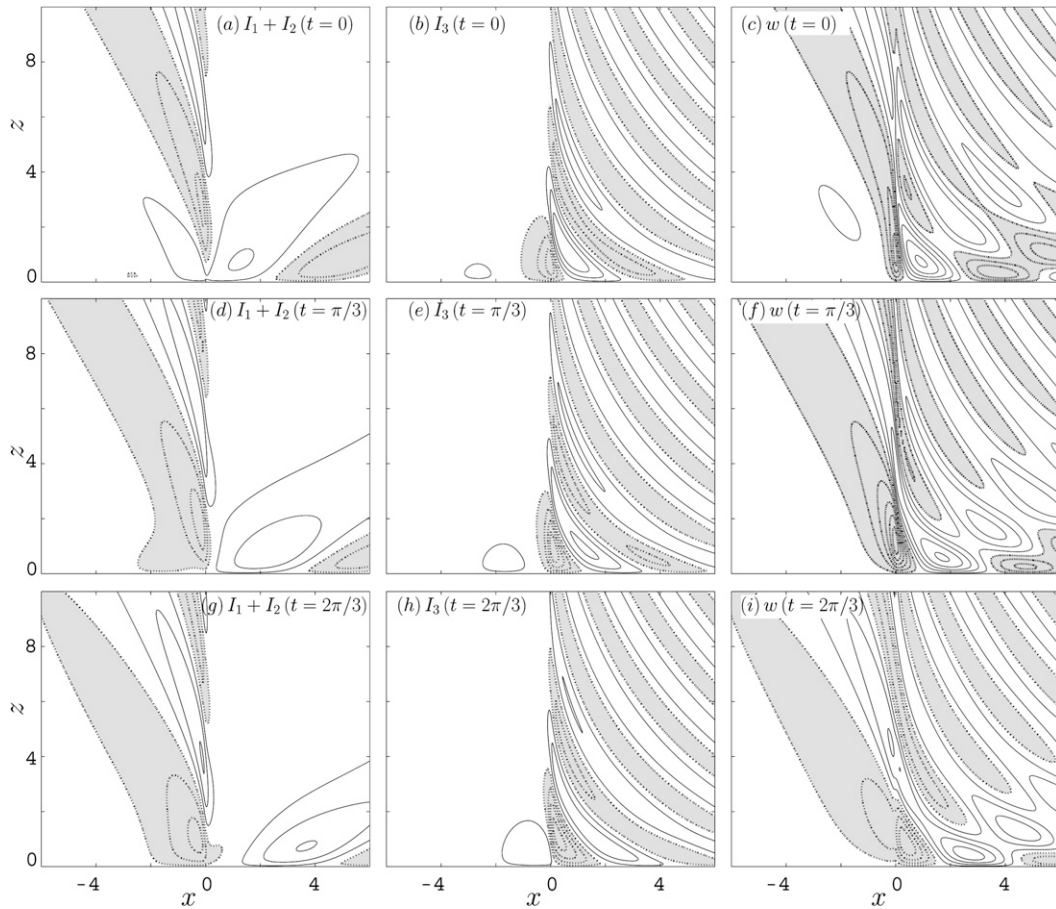
FIG. 6. Time evolution of both decomposed and total vertical velocity w (c.i. = 0.04) with $\mathcal{U} = 0.875$ and $\mathcal{L} = 0.1$. Sum of I_1 and I_2 modes at $t =$ (a) 0, (d) $\pi/3$, and (g) $2\pi/3$. (b),(e),(h) As in (a),(d),(g), but for I_3 modes; (c),(f),(i) As in (a),(d),(g), but for total w.

modes (shown by the thick dashed line in Figs. 4a,d,g,j) is computed by setting $\lambda = 1$ [or $\kappa = 1/(1 - \mathcal{U})$] in (24). (For $\mathcal{U} > 1$ the R83 modes do not exist—because the maximum wavenumber of $m = 1/\mathcal{U}$ is less than 1—and we simply set $\theta = \pi/2$). Note that the R83 raypaths give a good sense of the maximum disturbance envelope even for relatively large $\mathcal{U}$.

b. I_2 modes

For the I_2 branch we have $\sigma = -1$ and $\lambda = -m < 0$. Solving (24) for the horizontal and the vertical wavenumbers then gives

$$\kappa = (1 - \sqrt{\tan\theta})/\mathcal{U} \quad \text{and} \quad m = (\sqrt{1/\tan\theta} - 1)/\mathcal{U}, \tag{26}$$

where θ must satisfy $0 < \theta < \pi/4$ to give positive κ and negative λ. Inspection of (26) indicates that both κ and m are zero at $\theta = \pi/4$ and increase as θ decreases. Shorter horizontal waves thus have less steep raypaths

and smaller vertical wavelengths. The largest horizontal wavenumber of $\kappa = 1/\mathcal{U}$ occurs at $\theta = 0$.

As for I_1, the solution for I_2 is dominated by modes with $m \sim 1$ (i.e., the R83 modes). The raypath for these R83 modes (shown by the thick dashed line in Figs. 4b,e,h,k) is computed by setting $\lambda = -1$ [or $\kappa = 1/(1 + \mathcal{U})$] in (24).

c. I_3 modes

For the I_3 branch we have $\sigma = -1$ and $\lambda = m > 0$. The horizontal and the vertical wavenumbers are then given by

$$\kappa = (\sqrt{\tan\theta} + 1)/\mathcal{U} \quad \text{and} \quad m = (1 + \sqrt{1/\tan\theta})/\mathcal{U}, \tag{27}$$

where θ satisfies $0 < \theta < \pi/2$ to give both positive κ and λ. The horizontal wavenumber increases with increasing θ, with a minimum value of $\kappa = 1/\mathcal{U}$ occurring at $\theta = 0$.
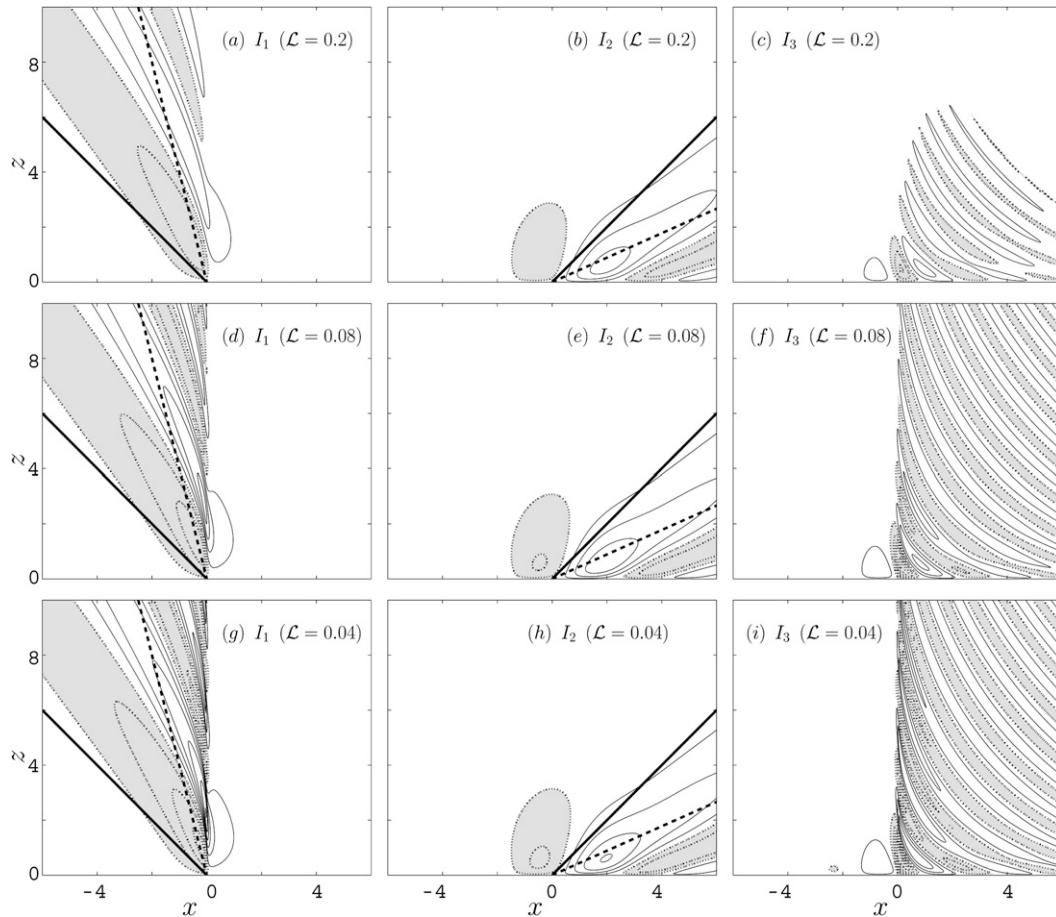
FIG. 7. Decomposition of w (c.i. = 0.04) into I_1, I_2, and I_3 branches for $\mathcal{U} = 0.5$ and varying $\mathcal{L}$ at time $t = \pi/2$. (a) I_1, (b) I_2, and (c) I_3 for coastal width $\mathcal{L} = 0.2$. (d)–(f) As in (a)–(c), but for $\mathcal{L} = 0.08$; (g)–(i) as in (a)–(c), but for $\mathcal{L} = 0.04$.

The vertical wavenumber decreases with θ, reaching $m = 1/\mathcal{U}$ at $\theta = \pi/2$.

Note that these results provide some insight into the differences between u and w as observed in Figs. 3 and 5. Specifically, the u field has more amplitude near $\kappa = \kappa_{\mathcal{U}}$ than does the w field [because $\partial\hat{\psi}/\partial z \to \infty$ as $\kappa \to \kappa_{\mathcal{U}}$ for I_2 and I_3; see the appendix]. As seen in (26) and (27), for I_2 and I_3 the $\kappa \sim \kappa_{\mathcal{U}}$ modes propagate close to the ground.

d. Discussion: Wave scales at large $\mathcal{U}$ and $\mathcal{U}/\mathcal{L}$

The group velocity results suggest that when $\mathcal{U}$ and $\mathcal{U}/\mathcal{L}$ are large, the dominant spatial scales in the solution are fundamentally different from those at $\mathcal{U} = 0$. For large $\mathcal{U}$, the I_1 part of the disturbance is found mainly over the coastline (cf. Fig. 4), and the dominant vertical scale for the I_1 branch is then $1/m \sim \mathcal{U}$. In dimensional terms this translates to U/N, which is also the scale for flow past a steady, nonoscillating source—that is, for large $\mathcal{U}$ the effect of flow past the local heating gradient dominates the diurnal oscillation.

The I_2 disturbance at large $\mathcal{U}$ is found mainly near $\theta = 0$ (cf. Fig. 4), where the dominant horizontal scale is $1/\kappa \sim \mathcal{U}$. In dimensional terms this scale is U/ω, which measures the distance traveled by a fluid particle during one oscillation cycle. The basis for this advective scale is seen most easily from (3). At $\theta = 0$ we have $w^* = 0$, so that (3) becomes

$$\frac{\partial b^*}{\partial t^*} + U \frac{\partial b^*}{\partial x^*} = Q^*,$$

showing that the buoyancy is simply advected at speed U while undergoing heating and cooling by the source. The anomaly at any point downstream thus retains a memory of the heating phase present when the particle first entered the coastal zone, and the distance between relatively warm and relatively cold particles is measured by the advective distance U/ω.

Finally, the spatial scales for I_3 (which dominates at large $\mathcal{U}/\mathcal{L}$) are the same as the large $\mathcal{U}$ limits for I_1 and I_2. That is, over the coastline the I_3 branch has a depth scale of U/N, while along $\theta = 0$ the length scale for I_3 is U/ω.
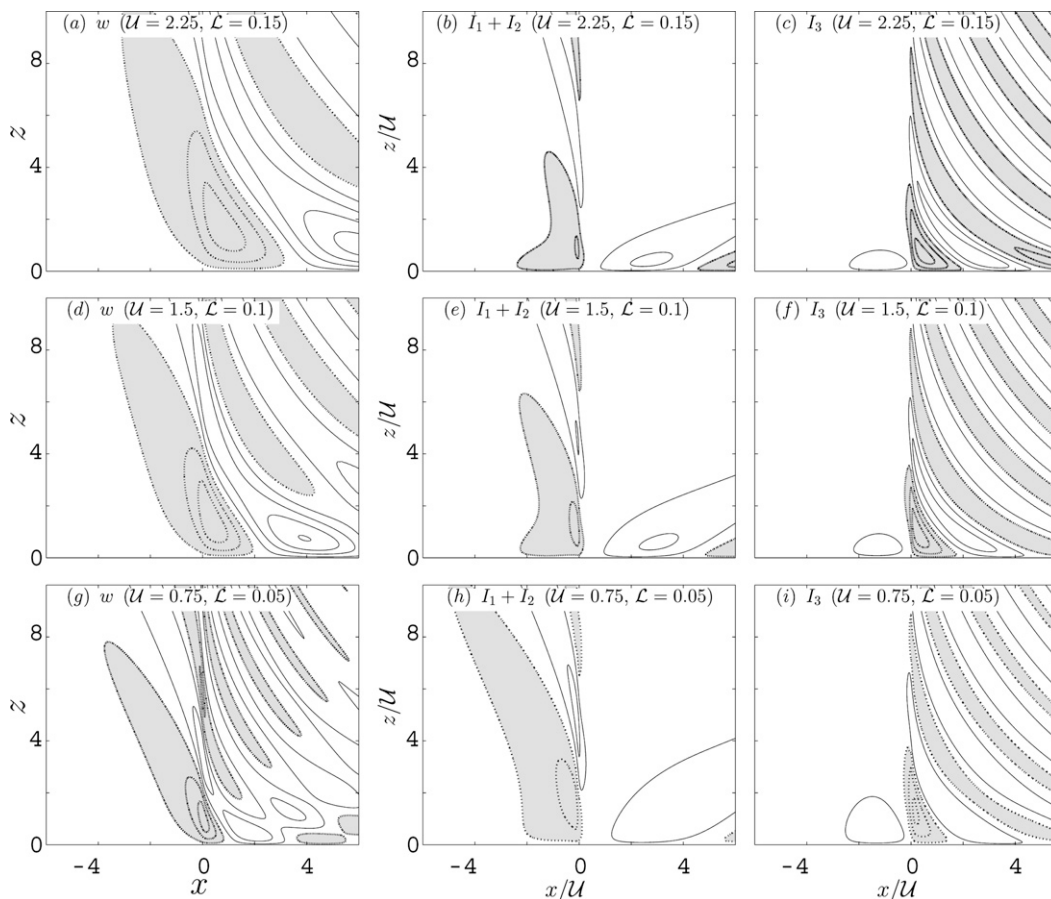
FIG. 8. Total w and decomposition into $I_1 + I_2$ and I_3 branches for fixed $\mathcal{U}/\mathcal{L} = 15$ at time $t = \pi/2$. (a) Total w, (b) $I_1 + I_2$, and (c) I_3 (c.i. = 0.0267) with $\mathcal{U} = 2.25$ and $\mathcal{L} = 0.15$. (d)–(f) As in (a)–(c), but for $\mathcal{U} = 1.5$ and $\mathcal{L} = 0.1$ (c.i. = 0.04); (g)–(i) as in (a)–(c), but for $\mathcal{U} = 0.75$ and $\mathcal{L} = 0.05$ (c.i. = 0.08). (a),(d),(g) use standard diurnal axis scalings, all other panels use modified large $\mathcal{U}$ and $\mathcal{U}/\mathcal{L}$ scalings. Contours vary with $1/\mathcal{L}$ to account for increased amplitude with decreasing $\mathcal{L}$.

These scales for large $\mathcal{U}$ and $\mathcal{U}/\mathcal{L}$ are illustrated by Fig. 8, which shows the w disturbance for varying values of $\mathcal{U}$ and $\mathcal{L}$, but with $\mathcal{U}/\mathcal{L}$ held fixed at 15. The first column of the figure shows the total fields as displayed with the standard diurnal axis scalings. The second and third columns show the $I_1 + I_2$ and I_3 decomposition as displayed on axes using the modified scales described above. As $\mathcal{U}$ increases, the fields in the first column expand spatially, reflecting the $\mathcal{U}$ dependence of the dominant spatial scales. But when rescaled with the appropriate large $\mathcal{U}$ and $\mathcal{U}/\mathcal{L}$ scalings, the disturbance structure is relatively uniform (apart from small changes in I_2 as $\mathcal{U}$ becomes sufficiently large).

It is worth pointing out that the importance of I_3 (as measured by the ratio of I_3 amplitude to $I_1 + I_2$ amplitude) in Fig. 8 is essentially constant. This reinforces the notion that the relative amount of power in I_3 is determined largely by $\mathcal{U}/\mathcal{L}$ (because $\mathcal{U}/\mathcal{L}$ in the figure is fixed).

6. Conclusions

Building on R83, this study has explored the linear wave response to a diurnally oscillating heating gradient in a background wind. This model can be considered a simple analog to the equatorial coastal circulation. Under a diurnal wave scaling, the wave response is a function of two control parameters: a nondimensional coastal width $\mathcal{L} = \omega L/NH$ and a nondimensional wind speed $\mathcal{U} = U/NH$.

For $\mathcal{U} \neq 0$ the Fourier integral solution consists of three distinct wave branches: I_1, I_2, and I_3. The I_1 and I_2 branches correspond directly to the two branches described by R83, except with Doppler shifting and associated tilting of the raypaths. The extent of this Doppler shifting is determined directly by $\mathcal{U}$, with larger $\mathcal{U}$ leading to greater raypath tilting and more widely dispersed wave energy.

The I_3 branch exists only for $\mathcal{U} \neq 0$ and is shown to be broadly similar to flow past a stationary heat source or a

topographic obstacle. The importance of this branch (relative to I_1 and I_2) increases as $\mathcal{U}/\mathcal{L}$ increases, with the amplitude becoming similar to the other two branches once $\mathcal{U}/\mathcal{L} \sim 2$. For typical dimensional parameters (such as those given in section 3c), a characteristic threshold wind for the importance of the I_3 mode is roughly $U \sim 1.5$ m s^{-1} (with smaller L implying smaller thresholds). For still larger $\mathcal{U}/\mathcal{L}$, the I_3 branch becomes the dominant part of the solution.

The spatial scales present in all three branches can be explained reasonably well using group velocity arguments. At large $\mathcal{U}$ and $\mathcal{U}/\mathcal{L}$, the dominant scales are fundamentally different from the $\mathcal{U} = 0$ case.

It should be emphasized that we do not expect our simple linear theory to provide an accurate description of the sea breeze in its entirety. Most notably, the model completely misses the low-level sea breeze front and the associated density current. However, it is reasonable to expect that the model provides some insight into the larger-scale wave response associated with the sea breeze. Such waves are difficult to observe directly but have been noted in some recent real-world modeling studies (e.g., Mapes et al. 2003b). There has also been speculation that such coastally generated gravity waves are involved in the observed diurnal propagation of convection off tropical coastlines (see Mapes et al. 2003a and Yang and Slingo 2001, among others). At the very least, the current study provides a simple conceptual reference point for the study of these waves.

APPENDIX

Computational Methods for I_2 and I_3

As noted in section 4a, the integrals I_2 and I_3 in (20) and (21) feature rapid oscillations in the integrands near $\kappa = \kappa_{\mathcal{U}}$. These oscillations lead to poor numerical resolution near the singularity, which in turn compromises the accuracy of the quadrature. The problem is particularly acute for $u = \partial\psi/\partial z$, because for u the amplitude is singular as well as the phase.

To address this problem we use a method first introduced by Muraki (2000) in the context of rotating flow past topography. Details of the method are given below.

However, we begin by briefly describing the more conventional methods used for I_1.

a. Computation of I_1

Inspection of (19) shows that the integrand is well behaved for all $\kappa > 0$; computation of the integral is therefore straightforward. In the present study we use the substitution $\kappa = \kappa_1(1/s - 1)$ to map the indefinite interval $0 \leq \kappa < \infty$ to the finite range $0 < s \leq 1$. A quadrature using the trapezoidal rule is applied using a uniform discretization in s. Varying the parameter κ_1 shifts the point density to smaller or larger κ, with half the total points at $\kappa < \kappa_1$ and half at larger κ. The choice $\kappa_1 = 5$ was found to give reasonable results with modest effort.

b. Desingularization for I_2 and I_3

To account for the singularities in I_2 and I_3, we use two approaches in combination. First we identify an integrable function whose behavior at the singular point matches that of the function to be integrated. Subtracting this matching function from the integrand then effectively damps the singularity. The second step is to then stretch the remaining singular oscillation using an appropriate coordinate mapping.

To illustrate, we consider our most singular case, specifically the I_3 contribution to the horizontal velocity u. Taking a vertical derivative of (21) gives

$$\frac{\partial I_3}{\partial z} = -\frac{1}{2\pi}\int_{\kappa_{\mathcal{U}}}^{\infty}\frac{e^{-\kappa\mathcal{L}}}{\kappa^2 + (\mathcal{U}\kappa - 1)^2}e^{i(\kappa x - t)}(im\,e^{imz} + e^{-z})\,d\kappa,$$

(A1)

where $m = \kappa/(\mathcal{U}\kappa - 1)$. The second term in the last parentheses is well behaved, but the $im\,e^{imz}$ term has both phase and amplitude singularities as $\kappa \rightarrow \kappa_{\mathcal{U}}^+$.

To transform to a finite range we use the trigonometric substitution

$$\kappa = \kappa_{\mathcal{U}}\frac{1}{1 - \sin\theta},$$

which maps (A1) to

$$\frac{\partial I_3}{\partial z} = -\frac{1}{2\pi\kappa_{\mathcal{U}}}\int_0^{\pi/2}C_3(\theta)\,e^{-z}\cos\theta\,d\theta$$
$$-\frac{i}{2\pi}\int_0^{\pi/2}C_3(\theta)\,\exp\left(i\kappa_{\mathcal{U}}z\csc\theta\right)\cot\theta\,d\theta,\quad\text{where}$$

(A2)

$$C_3(\theta) = \frac{\kappa^2 e^{-\kappa\mathcal{L}}}{\kappa^2 + (\mathcal{U}\kappa - 1)^2}e^{i(\kappa x - t)}$$
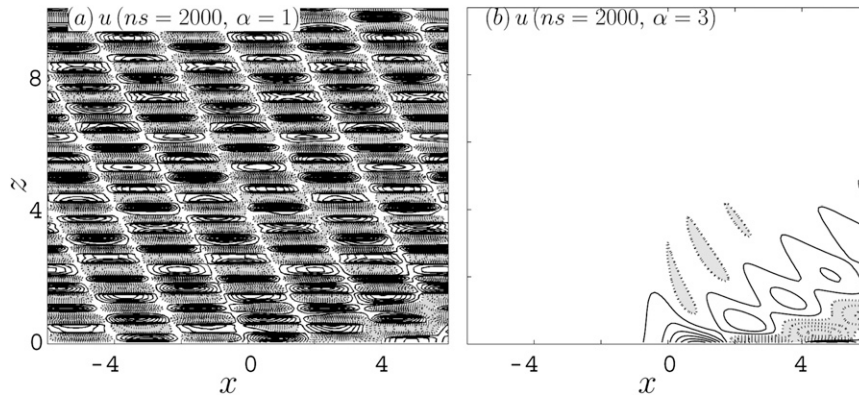
FIG. A1. Horizontal velocity u with $\mathcal{U} = 0.625$ and $\mathcal{L} = 0.1$ at time $t = \pi/2$. (a) Direct quadrature of (A2) with 2000 points and $\alpha = 1$. (b) Desingularized quadrature of (A4) with 2000 points and $\alpha = 3$.

is a well-behaved amplitude factor. The first integral in (A2) can be directly discretized without problems. However, the second integral inherits the original phase and amplitude singularities as $\theta \to 0^+$.

To remove these singularities, we note that sufficiently near the singular point the integrand in (A2) matches that of a tabulated integral, specifically the exponential integral E_1 (e.g., Abramowitz and Stegun 1972, section 5.1). That is, with a change of variable (Muraki 2000) the exponential integral can be written for $\mathrm{Re}(\xi) \geq 0$ as

$$E_1(\xi) = \int_0^{\pi/2} \exp(-\xi \csc \theta) \cot \theta \, d\theta, \qquad \text{(A3)}$$

which for imaginary ξ has the same singular phase and amplitude behavior as (A2). Combining (A2) with (A3) then gives

$$\begin{aligned}
\frac{\partial I_3}{\partial z} = &- \frac{1}{2\pi\kappa_{\mathcal{U}}} \int_0^{\pi/2} C_3(\theta) e^{-z} \cos \theta \, d\theta \\
&- \frac{i}{2\pi} \int_0^{\pi/2} A_3(\theta) \exp(i\kappa_{\mathcal{U}} z \csc \theta) \cot \theta \, d\theta \\
&- \frac{i}{2\pi} C_3(0) E_1(-i\kappa_{\mathcal{U}} z)
\end{aligned} \qquad \text{(A4)}$$

where the difference amplitude

$$A_3(\theta) = C_3(\theta) - C_3(0)$$

now has a first-order zero at $\theta = 0^+$ so that $A_3(\theta)\cot\theta$ remains finite.

Because of the $\cot\theta$ term in (A2), the subtraction step in (A4) damps the amplitude singularity but leaves a finite-amplitude singular oscillation. To regularize this oscillation we apply a second coordinate mapping

$$\theta = \frac{\pi}{2} s^{\alpha}, \qquad \text{(A5)}$$

with s ranging from 0 to 1. Setting $\alpha > 1$ causes the singular oscillation near $\theta = 0^+$ to be stretched, in the sense that $d\theta = \alpha(\pi/2)s^{\alpha-1} ds \to 0$ as $s \to 0$. The resulting integrand for $0 \leq s \leq 1$ then has an order $\alpha - 1$ zero at the singular endpoint.

Finally, the desingularized integral (A4) with (A5) is computed with a trapezoidal quadrature using a uniform discretization in s. Similar methods are used to compute the I_2 integral for u as well as the w integrals (which are one order less singular in amplitude and thus easier to compute).

c. An example

Figure A1 shows an example calculation for the case $\mathcal{U} = 0.625$ with $\mathcal{L} = 0.1$. Shown in Fig. A1a is a direct quadrature of (A2)—that is, without the subtraction step in (A4) and with $\alpha = 1$ in (A5)—using a uniform discretization of $ns = 2000$ points. The analogous desingularized quadrature of (A4) with $\alpha = 3$ and $ns = 2000$ is shown in Fig. A1b. As can be seen, the direct trapezoidal quadrature of (A2) features significant numerical artifacts due to the singular nature of the integrand. By contrast, in the desingularized case these artifacts are effectively removed.

REFERENCES

Abramowitz, M., and I. A. Stegun, 1972: *Handbook of Mathematical Functions*. 9th ed. Dover, 1046 pp.

Carbone, E. R., J. D. Tuttle, D. A. Ahijevych, and S. B. Trier, 2002: Inferences of predictability associated with warm season precipitation episodes. *J. Atmos. Sci.,* **59,** 2033–2056.

Cenedese, A., M. Miozzi, and P. Monti, 2000: A laboratory investigation of land and sea breeze regimes. *Exp. Fluids,* **29,** 291–299.

Dalu, G. A., and R. A. Pielke, 1989: An analytical study of the sea breeze. *J. Atmos. Sci.,* **46,** 1815–1825.

Davis, W. M., G. Schultz, and R. D. Ward, 1889: An investigation of the sea-breeze. *New Engl. Meteor. Soc. Obs.,* **21,** 214–264.

Defant, F., 1951: Local winds. *Compendium of Meteorology,* T. F. Malone, Ed., Amer. Meteor. Soc., 655–672.

Estoque, M. A., 1961: A theoretical investigation of the sea breeze. *Quart. J. Roy. Meteor. Soc.,* **87,** 136–146.

Finkele, K., J. M. Hacker, H. Kraus, and R. A. D. Byron-Scott, 1995: A complete sea-breeze circulation cell derived from aircraft observations. *Bound.-Layer Meteor.,* **73,** 299–317.

Fisher, E. L., 1960: An observational study of the sea breeze. *J. Meteor.,* **17,** 645–660.

——, 1961: A theoretical study of the sea breeze. *J. Meteor.,* **18,** 216–233.

Halley, E., 1686: An historical account of the trade winds, and monsoons, observable in the seas between and near the tropicks, with an attempt to assign physical cause of said winds. *Philos. Trans. Roy. Soc. London.,* **16,** 153–168.

Haurwitz, B., 1947: Comments on the sea-breeze circulation. *J. Meteor.,* **4,** 1–8.

Jeffreys, H., 1922: On the dynamics of wind. *Quart. J. Roy. Meteor. Soc.,* **48,** 29–46.

Koch, S. E., F. Zhang, M. L. Kaplan, Y.-L. Lin, R. Weglarz, and C. M. Trexler, 2001: Numerical simulation of a gravity wave event over CCOPE. Part III: The role of a mountain–plains solenoid in the generation of the second wave episode. *Mon. Wea. Rev.,* **129,** 909–933.

Lin, Y.-L., 2007: *Mesoscale Dynamics.* Cambridge University Press, 674 pp.

Mapes, B. E., T. T. Warner, M. Xu, and A. J. Negri, 2003a: Diurnal patterns of rainfall in northwestern South America. Part I: Observations and context. *Mon. Wea. Rev.,* **131,** 799–812.

——, ——, and M. Xu, 2003b: Diurnal patterns of rainfall in northwestern South America. Part III: Diurnal gravity waves and nocturnal convection offshore. *Mon. Wea. Rev.,* **131,** 830–844.

Miller, S. T. K., B. D. Keim, R. W. Talbot, and H. Mao, 2003: Sea breeze: Structure, forecasting, and impacts. *Rev. Geophys.,* **41,** 1–31.

Muraki, D. J., 2000: Revisiting Queney's flow over a mesoscale ridge. Preprints, *Ninth Conf. on Mountain Meteorology,* Aspen, CO, Amer. Meteor. Soc., 5.3.

Pearce, R. P., 1955: The calculation of a sea-breeze circulation in terms of the differential heating across the coast line. *Quart. J. Roy. Meteor. Soc.,* **81,** 351–391.

——, R. C. Smith, and J. S. Malkus, 1956: The calculation of a sea-breeze circulation in terms of the differential heating across the coast line. *Quart. J. Roy. Meteor. Soc.,* **82,** 235–241.

Pierson, W. J., 1950: The effects of eddy viscosity, Coriolis deflection, and temperature fluctuation on the sea breeze as a function of time and height. Ph.D. thesis, College of Engineering, New York University, 30 pp.

Puygrenier, V., F. Lohou, B. Campistron, F. Saïd, G. Pigeon, B. Bénech, and D. Serça, 2005: Investigation on the fine structure of sea-breeze during ESCOMPTE experiment. *Atmos. Res.,* **74,** 329–353.

Rotunno, R., 1983: On the linear theory of the land and sea breeze. *J. Atmos. Sci.,* **40,** 1999–2009.

Schmidt, F. H., 1947: An elementary theory of the land- and sea-breeze circulation. *J. Meteor.,* **4,** 9–15.

Simpson, J. E., 1997: *Gravity Currents in the Environment and the Laboratory.* 2nd ed. Cambridge University Press, 244 pp.

Sun, W. Y., and I. Orlanski, 1981: Large-scale convection and sea breeze circulation. Part I: Stability analysis. *J. Atmos. Sci.,* **38,** 1675–1693.

Walsh, J. E., 1974: Sea breeze theory and applications. *J. Atmos. Sci.,* **31,** 2012–2026.

Yan, H., and R. A. Anthes, 1987: The effect of latitude on the sea breeze. *Mon. Wea. Rev.,* **115,** 936–956.

Yang, G., and J. Slingo, 2001: The diurnal cycle in the tropics. *Mon. Wea. Rev.,* **129,** 784–801.

Zhang, F., and S. E. Koch, 2000: Numerical simulation of a gravity wave event over CCOPE. Part II: Waves generated by an orographic density current. *Mon. Wea. Rev.,* **128,** 2777–2796.